ADVANCED MATERIALS INTERFACES
www.advmatinterfaces.de

Two-Step Solution-Processed Two-Component Bilayer Phthalocyaninato Copper-Based Heterojunctions with Interesting Ambipolar Organic Transiting and Ethanol-Sensing Properties

Yanling Wu, Pan Ma, Ningan Wu, Xia Kong, Marcel Bouvet, Xiyou Li, Yanli Chen, and Jianzhuang Jiang**

The two-component phthalocyaninato copper-based heterojunctions fabricated from *n*-type CuPc($COOC_8H_{17}$)$_8$ and *p*-type CuPc(OC_8H_{17})$_8$ by a facile two-step solution-processing quasi-Langmuir–Shäfer method with both *n*/*p*- and *p*/*n*-bilayer structures are revealed to exhibit typical ambipolar air-stable organic thin-film transistor (OTFT) performance. The *p*/*n*-bilayer devices constructed by depositing CuPc($COOC_8H_{17}$)$_8$ film on CuPc(OC_8H_{17})$_8$ sub-layer show superior OTFT performance with hole and electron mobility of 0.11 and 0.02 cm^2 V^{-1} s^{-1}, respectively, over the ones with *n*/*p*-bilayer heterojunction structure with the hole and electron mobility of 0.03 and 0.016 cm^2 V^{-1} s^{-1} due mainly to the more intense face-to-face π–π interaction in the CuPc(OC_8H_{17})$_8$ sub-layer than that in CuPc($COOC_8H_{17}$)$_8$ sub-layer, revealing the effect of different stacking sequence on tuning the OTFT performance of phthalocyanine-based bilayer heterojunctions. Furthermore, the chemiresistive devices fabricated from the *p*/*n*-bilayer heterojunction, with both Au and Indium tin oxide (ITO) interdigitated electrodes (IDEs), also display much better sensing properties to ethanol than those with *n*/*p*-bilayer heterojunction in terms of sensitivity and reversibility. Significantly, time-dependent current plot of the *p*/*n*-bilayer heterojunction with ITO IDEs reveals a detection limit as low as 100 ppm, nearly complete reversibility, and high selectivity to ethanol even at room temperature, rendering this novel two-component heterojunction device a great application potential in practical detecting ethanol.

1. Introduction

Ambipolar organic thin-film transistors (OTFTs) allowing dual operation of both *p* and *n* types with solution-processability that ensure low-cost fabrication have attracted increasing research interests in the past decade due to their great practical application potential in low-cost integrated circuits like high gain complementary metal-oxide-semiconductor inverters and light emitting devices.[1,2] Initial attention in this direction has been focused on the single-component ambipolar organic semiconductors.[3] However, associated with the intrinsic nature of common organic semiconductors with conjugated electronic structure, it is very hard to modulate both their highest occupied molecular orbital (HOMO) and lowest unoccupied molecular orbital (LUMO) energy levels to simultaneously meet the working electrode potential so as to act as good ambipolar organic semiconductors with simultaneous high and balanced carrier mobility for both holes and electrons for single-component

Y. Wu, N. Wu, X. Kong, Prof. X. Li, Prof. Y. Chen, Prof. J. Jiang
School of Science
China University of Petroleum (East China)
Qingdao 266580, China
E-mail: yanlichen@upc.edu.cn; jianzhuang@ustb.edu.cn
Prof. J. Jiang
Beijing Key Laboratory for Science and Application of Functional Molecular and Crystalline Materials
Department of Chemistry
University of Science and Technology Beijing
Beijing 100083, China

Dr. P. Ma
Jinan Academy of Agricultural Sciences
Jinan 250316, China
Prof. M. Bouvet
Institut de Chimie Moléculaire de l'Université de Bourgogne (ICMUB)
CNRS UMR 5260, Dijon cedex 21078, France

DOI: 10.1002/admi.201600253

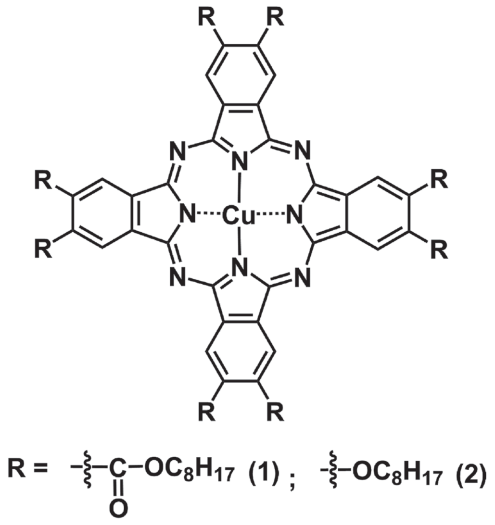

Scheme 1. Schematic molecular structures of $CuPc(COOC_8H_{17})_8$ (**1**) and $CuPc(OC_8H_{17})_8$ (**2**).

OTFT devices.[4] This inspired the scientists in this field to try to fabricate the ambipolar OTFTs using two organic components.[5] As early as in 1995, the first two-component bilayer thin film field transistor was prepared from *p*-type hexathienylene and *n*-type C_{60} with the help of vacuum deposition technique, which indeed displayed the expected ambipolar device performance with the carrier mobility of 4×10^{-3} cm^2 V^{-1} s^{-1} for holes and 5×10^{-3} cm^2 V^{-1} s^{-1} for electrons, respectively.[6] In 2006, vacuum-deposited bilayer-based OTFTs were fabricated from the *p*-type CuPc as the first layer and *n*-type $F_{16}CuPc$ as the second layer, showing the ambipolar charge transport with both electron and hole mobilities in the order of 10^{-4} cm^2 V^{-1} s^{-1}.[7] Interestingly, fabrication of the same $F_{16}CuPc$/CuPc heterojunction devices by means of solution-processed Langmuir–Blodgett CuPc film instead of vacuum-deposited CuPc layer as the first layer led to an obvious improvement in the carrier mobilities to the order of 10^{-3} cm^2 V^{-1} s^{-1} for both holes and electrons due to the improved molecular alignment in the semiconducting layers.[8] Very recently, a novel two-component bilayer heterojunction OTFT device was constructed by directly growing ambipolar (TFPP)Eu[Pc(OPh)$_8$]Eu[Pc(OPh)$_8$] film onto the vacuum deposited *p*-type CuPc film, affording the best result for ambipolar bilayer OTFTs with balanced and meanwhile quite good carrier mobilities of 0.30 and 0.16 cm^2 V^{-1} s^{-1} for holes and electrons, respectively, which is even significantly better in comparison with that of the single-component OTFT device fabricated from (TFPP)Eu[Pc(OPh)$_8$]Eu[Pc(OPh)$_8$] film with hole mobility of 6×10^{-5} cm^2 V^{-1} s^{-1} and electron mobility of 1.4×10^{-4} cm^2 V^{-1} s^{-1}.[9] However, despite the effort paid thus far, great challenges like the development of low-cost solution-processed technique to fabricate two-component bilayer heterojunction OTFTs and understanding the effect of the interface structure on the device performance still remain in this direction.[10]

In the present paper, the two-component heterojunctions were fabricated from *n*-type semiconducting $CuPc(COOC_8H_{17})_8$ (**1**) and *p*-type semiconducting $CuPc(OC_8H_{17})_8$ (**2**) by a facile two-step solution-processing quasi-Langmuir–Shäfer (QLS) method with both *p*/*n*-[$CuPc(OC_8H_{17})_8$/$CuPc(COOC_8H_{17})_8$] and *n*/*p*-[$CuPc(COOC_8H_{17})_8$/$CuPc(OC_8H_{17})_8$] bilayer structures (**Schemes 1** and **2**), exhibiting typical ambipolar air-stable OTFT performance. The *p*/*n*-bilayer devices constructed by depositing $CuPc(COOC_8H_{17})_8$ film on the $CuPc(OC_8H_{17})_8$ sub-layer showed superior OTFT performance with hole and electron mobility of 0.11 and 0.02 cm^2 V^{-1} s^{-1}, respectively, over the ones with *n*/*p*-bilayer heterojunction structure with the hole and electron mobility of 0.03 and 0.016 cm^2 V^{-1} s^{-1} due mainly to the more intense face-to-face π–π interaction in the $CuPc(OC_8H_{17})_8$ sub-layer than that in $CuPc(COOC_8H_{17})_8$ sub-layer, indicating the important role of the sub-layer internal structure toward improving the molecular ordering and domain connectivity in the top-layer film in the two-component heterojunction OTFT devices. Nevertheless, the chemiresistive devices fabricated from the *p*/*n*-bilayer heterojunction, with both Au and Indium tin oxide (ITO) interdigitated electrodes (IDEs), also display much better sensing properties to ethanol than those with *n*/*p*-bilayer heterojunction structure in terms of sensitivity and reversibility, in the concentration range of 100–1400 ppm: Time-dependent current plot of the *p*/*n*-bilayer heterojunction chemiresistive devices with ITO IDEs reveals a detection limit as low as 100 ppm, nearly complete reversibility, and high selectivity to ethanol even at room temperature, rendering this novel two-component heterojunction device a great application potential in practical detecting ethanol.

At the end of this section, it is worth noting that due to the wide range of applications in biomedical, chemical, medical, and food industries in particular in the drink-drive limit

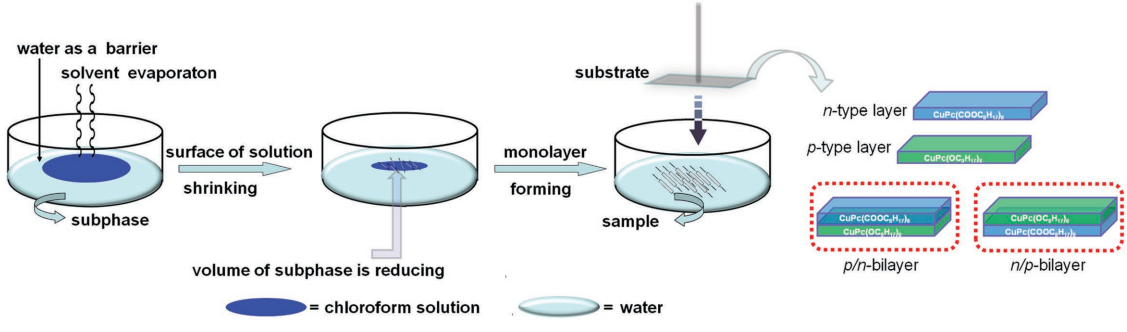

Scheme 2. Preparation of the single-component monolayer film and two-component bilayer heterojunction film by the quasi-Langmuir–Shäfer (QLS) procedure.

Table 1. OTFT characteristics for the single component [CuPc($COOC_8H_{17}$)$_8$, CuPc(OC_8H_{17})$_8$] and two-component *p*/*n*- and *n*/*p*-bilayer heterojunction film devices.

	n-channel OTFT			*p*-channel OTFT		
	μ_e [cm^2 V^{-1} s^{-1}]	On/off ratio	V_{th} [V]	μ_h [cm^2 V^{-1} s^{-1}]	On/off ratio	V_{th} [V]
CuPc($COOC_8H_{17}$)$_8$	0.22(N_2)	10^2	−5	No observation		
CuPc(OC_8H_{17})$_8$	No observation			0.20	10^2	+0.5
p/*n*-bilayer	0.02	10^3	−2.5	0.11	10^3	+0.1
n/*p*-bilayer	0.016	10^2	−2.5	0.03	10^2	+2.5

detecting,[11–13] ethanol sensors with high sensitivity and selectivity as well as fast response and recovery time at a relative low working temperature are highly desired. Efforts paid thus far in this field led to the development of inorganic semiconductor (V_2O_5, SnO_2, TiO_2, Fe_2O_3, ZnO, CuO) based ethanol chemosensors with rather high sensitivity, which however suffer from the high working temperature (200–400 °C) and cross-sensitivity to other gases.[14] This in turn limits their practical applications. It is worth noting again that corresponding sensors used as a breath alcohol checker need to possess high sensitivity and selectivity in addition to the convenient detection for a low-level ethanol vapor in a complicated practical environment. Common inorganic semiconductor-based sensors developed thus far, however, cannot meet these requirements. As a consequence, both new ethanol-sensing organic materials and simple fabricating methods for preparing sensor devices are highly desired in this field.

2. Results and Discussions

2.1. Electrochemical Properties

Differential pulse voltammograms measurement over compounds **1** and **2** in CH_2Cl_2 disclosed two reversible one-electron redox couples with the first oxidation and first reduction potential at +1.14 and −0.49 V for **1** and +0.75 and −0.79 V (vs SCE) (SCE:Saturated Calomel Electrode) for **2**, respectively (Figure S1 and Table S1, Supporting Information). Accordingly, their HOMO and LUMO energy levels were estimated to be about −5.58 and −3.95 eV for **1** (with a band gap of 1.63 eV) and −5.18 and −3.65 eV for **2** (with a band gap of 1.43 eV), respectively.[3b] Investigations have revealed that the HOMO energy of good *p*-type organic materials should align with the work function of the source–drain electrodes (Au: 5.1 eV) to decrease the hole injection barrier.[15] As for the *n*-type molecular semiconductors, the LUMO energy for effective electron injection and stable charge transport under ambient conditions should locate below −4.0 eV.[16,17] To achieve good performance and air-stable ambipolar OTFT devices, molecular semiconductors simultaneously possessing appropriate HOMO (around the work function of Au electrode, 5.1 eV) and LUMO (below −4.0 eV) energy levels with their gap in the range of ≈1.0 eV are necessary. Obviously, in the present case compound **1** having electron-withdrawing octyloxycarbony substituents at the phthalocyanine periphery with the LUMO level of −3.95 eV suggests its potential *n*-type semiconductor nature. In good contrast, compound **2** with the HOMO energy level of −5.18 eV matches much better with the work function of gold (−5.1 eV) than **1** with the HOMO energy level of −5.58 eV, indicating its potential *p*-type semiconducting nature. In particular, these results clearly reveal the great potential for the fabrication of two-component bilayer heterojunction OTFT devices with ambipolar electrical characteristics using CuPc($COOC_8H_{17}$)$_8$ and CuPc(OC_8H_{17})$_8$ as *n*- and *p*-type semiconducting component, respectively.

2.2. OTFT Properties

To directly reveal/confirm the majority carrier type and corresponding mobility of these two compounds, typical top-contact/bottom-gate configuration OTFT devices have been fabricated from CuPc($COOC_8H_{17}$)$_8$ (**1**) and CuPc(OC_8H_{17})$_8$ (**2**) on the hexamethyldisilazane (HMDS)-treated SiO_2/Si substrate using the QLS technique. As shown in Figures S2 and S3 (Supporting Information) and **Table 1** and in line with previous result,[18] devices fabricated from **1** indeed show typically *n*-channel unipolar characteristics with the electron mobility of 0.22 cm^2 V^{-1} s^{-1} (measured in the nitrogen glove box). This is also true for those of **2** with typically *p*-channel unipolar characteristics and hole mobility of 0.20 cm^2 V^{-1} s^{-1} in air. It is worth noting that due to the improved film connectivity and quality, the device performance of **1** in the present case was found to be significantly improved with the electron mobility increased by about three orders of magnitude in comparison with the devices constructed from the self-assembled aggregates of the same compound.[18]

As a natural result of the clear demonstration of the majority *n*- and *p*-carrier type for CuPc($COOC_8H_{17}$)$_8$ (**1**) film on the CuPc(OC_8H_{17})$_8$ (**2**), respectively, the two-component bilayer heterojunction OTFTs were then fabricated by directly growing the CuPc($COOC_8H_{17}$)$_8$ or CuPc(OC_8H_{17})$_8$ film over the sublayer film of CuPc(OC_8H_{17})$_8$ or CuPc($COOC_8H_{17}$)$_8$ film using a two-step solution-based QLS method (Scheme 2). As shown in **Figure 1** and Table 1 and Figures S4 and S5 (Supporting Information), the bilayer heterojunction devices with both *p*/*n*- and *n*/*p*-structure display typical ambipolar electrical characteristics, representing the first solution-processed two-small-molecular-component bilayer heterojunction ambipolar OTFTs with good device performance. However, the *p*/*n*-bilayer devices exhibit better performance over the *n*/*p*-bilayer ones in terms of the carrier mobilities, 0.11 and 0.02 cm^2 V^{-1} s^{-1} for holes and electrons versus 0.03 and 0.016 cm^2 V^{-1} s^{-1}, indicating the

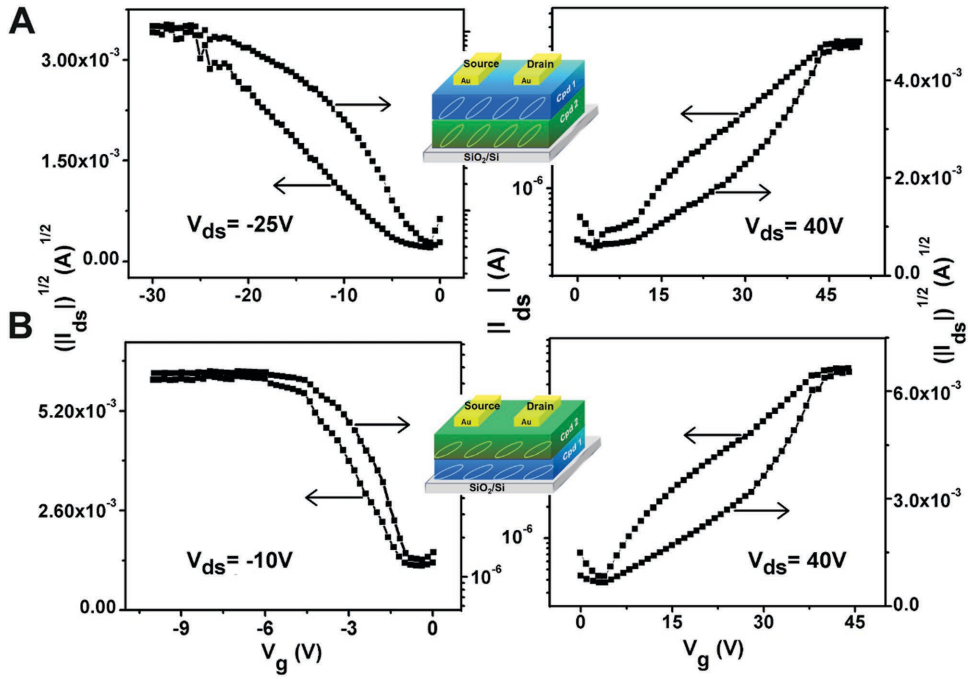

Figure 1. I_{ds}–V_g transfer characteristics of A) CuPc$(OC_8H_{17})_8$/CuPc$(COOC_8H_{17})_8$ bilayer (*p*/*n*-bilayer) and B) CuPc$(COOC_8H_{17})_8$/CuPc$(OC_8H_{17})_8$ bilayer (*n*/*p*-bilayer) heterojunction devices deposited on the HMDS-treated SiO_2/Si (300 nm) substrates measured in ambient conditions. The inset shows the schematic representation of the bilayer architecture in OTFTs.

important role of the sub-layer film structure and quality in determining the top-layer film structure and quality and in turn the whole two-component bilayer heterojunction OTFT device performance as detailed below.

2.3. Thin Film Microstructures and Morphologies

It has been revealed that the conductive channels are at the interface between the top- and sub-layer of the two-component bilayer heterojunction.[7,9] For the purpose of clarifying the relationship between carrier mobilities and the interface structure of the two-component heterojunction devices, inspection over the molecular packing mode of either CuPc$(COOC_8H_{17})_8$ or CuPc$(OC_8H_{17})_8$ molecules in both the single- and two-component bilayer QLS films and the internal film-structure in the latter two-component bilayer QLS films has been carried out on the basis of the UV–vis absorption spectroscopy, thin-film X-ray diffraction (XRD), and AFM (Atomic Force Microscope) observations. As shown in **Figure 2** and Table S2 (Supporting Information), compounds **1** and **2** in chloroform solution display typical electronic absorption spectra for monomeric phthalocyaninato metal complexes with Soret and the main Q bands at 350 and 687 nm for **1**, respectively, and 340 and 680 nm for **2**.[18,19] The weak band appearing at 422 nm in the electronic absorption spectrum of **2** is attributed to the *n*–π^* transitions due to the lone pair of electron of oxygen atom.[20] In comparison with CuPc$(OC_8H_{17})_8$ (**2**), the absorptions of CuPc$(COOC_8H_{17})_8$ (**1**) in chloroform are considerably red-shifted as a result of the introduction of electron-withdrawing octyloxycarbony substituents at the Pc peripheral positions. However, after being fabricated into the QLS films (Figure 2) the absorptions of **1** and **2** due to the π–π^* transitions of phthalocyanine macrocycle appear in the visible region as a doublet at 650 and 735 nm for **1**, respectively, and 620 and 737 nm for **2** due to the Davydov splitting.[21] In addition, the band at higher energy side, 650 and 620 nm, is more intense than the lower energy band at 735 and 737 nm for both **1** and **2**, suggesting a typical α-CuPc phase (a special aggregation structure in which the planar phthalocyanine molecules are arranged in 1D π stacks)[9,21–23] and indicating the quite good quality of the multilayer films fabricated from **1** and **2** by means of the simple QLS thin-film deposition technique. As shown in **Scheme 3**. Furthermore, the QLS film of **2** shows more marked Davydov splitting in the Q absorption band (≈117 nm) than that of **1** (≈90 nm) (Figure 2), indicating the more intense intermolecular interactions either within the 1D π stack or between the neighboring π stacks in the QLS film of **2** than that of **1**. Actually, both alkoxycarbonyl and alkoxy side chains grafted on the phthalocyanine periphery are not polar enough to anchor the macrocycle parallel to the water surface, the macrocycles of both **1** and **2** are then tilted with respect to the water surface and thus able to self-organize into columnar assemblies along with the vaporization of organic solvent during the QLS fabrication process.[7] Furthermore, a more significant increase can be found for the ratio of the intensities of A_{737}/A_{620} (0.88) of the Q absorptions of **2** than that for **1**, A_{735}/A_{650} = 0.65 in the QLS films, suggesting the more effective face-to-face π–π overlapping within the columnar assembly in the *J*-type aggregates of **2** than that for **1**.[24a,b] The orientation angle of the phthalocyanine ring with respect to the substrate in the QLS films of **1** and **2** was found to amount to 34.6° and 50.5°, respectively, according to

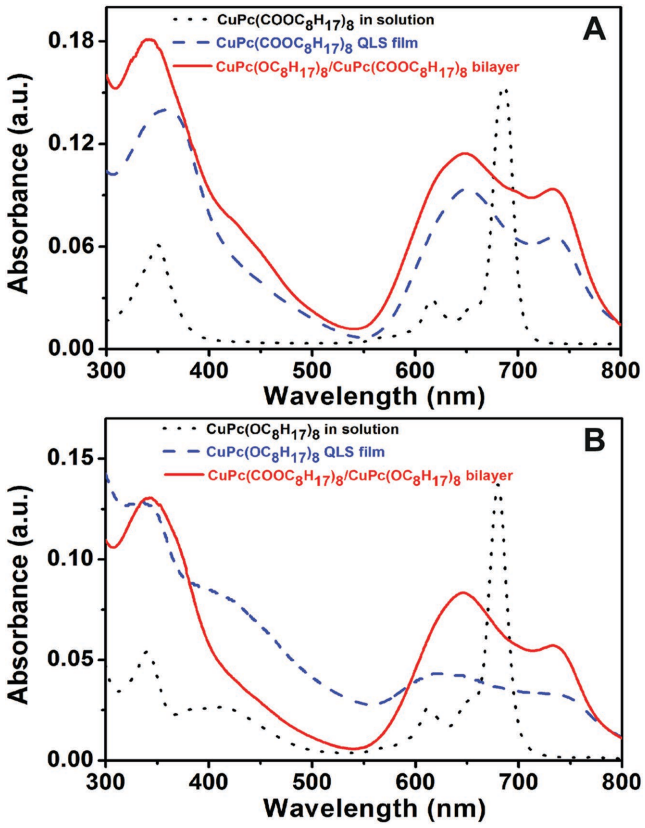

Figure 2. UV–vis absorption spectra of A) $CuPc(COOC_8H_{17})_8$ (**1**) in $CHCl_3$ solution (dotted line), $CuPc(COOC_8H_{17})_8$ QLS film (dashed line), and the $CuPc(OC_8H_{17})_8/CuPc(COOC_8H_{17})_8$ bilayer (*p*/*n*-bilayer) heterojunction thin film (solid line) and B) $CuPc(OC_8H_{17})_8$ (**2**) in $CHCl_3$ solution (dotted line), $CuPc(OC_8H_{17})_8$ QLS film (dashed line), and the $CuPc(COOC_8H_{17})_8/CuPc(OC_8H_{17})_8$ bilayer (*n*/*p*-bilayer) heterojunction thin film (solid line).

the polarized UV–vis measurements (Figure S6 and Table S3, Supporting Information),[24c] revealing the "edge-on" conformation (*J*-aggregation) of the phthalocyanine molecules in the QLS films of both **1** and **2**.[20b] In addition, the obvious larger orientation angle of the phthalocyanine ring with respect to the substrate for **2** suggests the more upright π–π stacking arrangement and more effective face-to-face π–π overlapping within the columnar assembly in the QLS film of **2** than that of **1**. This, in turn, becomes responsible for the better charge transport property revealed for the OTFTs fabricated from the QLS film of **2** than that of **1** as detailed above. At the end of this paragraph, it is worth mentioning that the splitting of the Q phthalocyanine band in the QLS film actually depends mainly on the interaction between the neighboring 1D phthalocyanine columns,[25] the larger Davydov splitting of the Q absorption band in the QLS film of **2** (≈117 nm) therefore suggests the more intense intermolecular interaction among neighboring phthalocyanine columns and the larger intercolumn distance in the QLS film of **2** than that of **1** (≈90 nm), which is further verified in an unambiguous manner by the thin-film XRD measurement result (vide infra).

As can be easily expected, both the two-component *p*/*n*- and *n*/*p*-bilayer heterojunction QLS films show just similar absorption feature in their UV–vis spectra to their single-component QLS films (Figure 2), indicating the similar "edge-on" conformation (*J*-aggregation) of the phthalocyanine molecules in these bilayer heterojunctions and single-component QLS films. Interestingly, slightly different Davydov splitting of the phthalocyanine Q band has been clearly disclosed between the *p*/*n*-type bilayer heterojunction film, 648 and 738 nm and the *n*/*p*-bilayer heterojunction film, 652 and 735 nm (Figure 2), due to the intrinsic different packing behavior between **1** and **2** in combination with the extrinsic different packing behavior of individual top-layer phthalocyanine molecules resulting from the surface structure/morphology of the sub-layer film in the bilayer heterojunction thin films.[9,26,27] This in turn results in the different device performance between the *p*/*n*- and the *n*/*p*-bilayer heterojunction OTFTs (vide supra).

The internal structure of the single-component and bilayer heterojunction thin films is further assessed using the out-of-plane (OOP) XRD technique. As shown in **Figure 3**A,B, in the low-angle range the OOP XRD patterns of $CuPc(COOC_8H_{17})_8$ (**1**) and $CuPc(OC_8H_{17})_8$ (**2**) QLS films exhibit only one sharp diffraction peak at 1.96 nm (2θ = 4.50°) and 2.51 nm (2θ = 3.52°), respectively, which corresponds to the monolayer thickness of the resulting QLS film (or the interstacking distance of the α-phase lattice planes), suggesting a regular lamella structure of either **1** or **2** formed in the QLS film.[28,29] As a consequence, the orientation angle of the phthalocyanine ring with respect to the substrate of 33° and 50° has been deduced for **1** and **2** with the help of the simulated molecular dimension of $CuPc(COOC_8H_{17})_8$ (3.6 nm) and $CuPc(OC_8H_{17})_8$ (3.3 nm).[30a] The result is in good accordance with that deduced on the basis of polarized UV–vis spectroscopic measurement as detailed above, confirming that the macrocycle molecules of **1** and **2** are

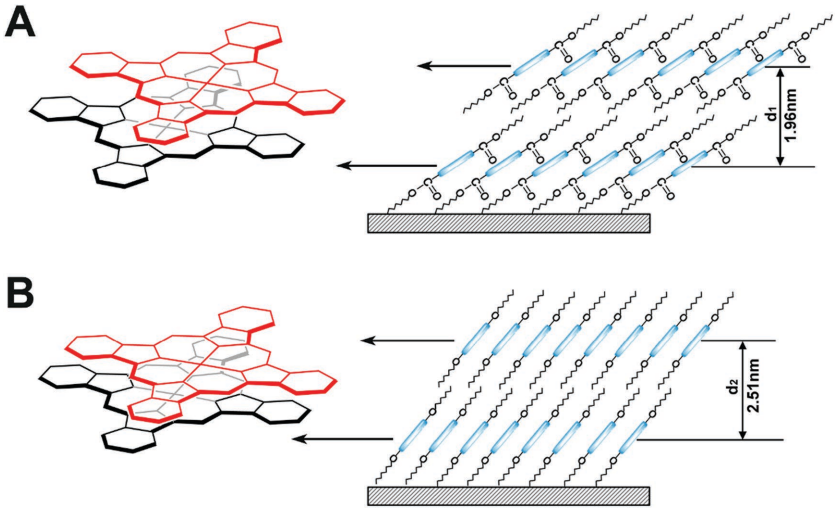

Scheme 3. Schematic molecular arrangement of A) **1** and B) **2** in the QLS films.

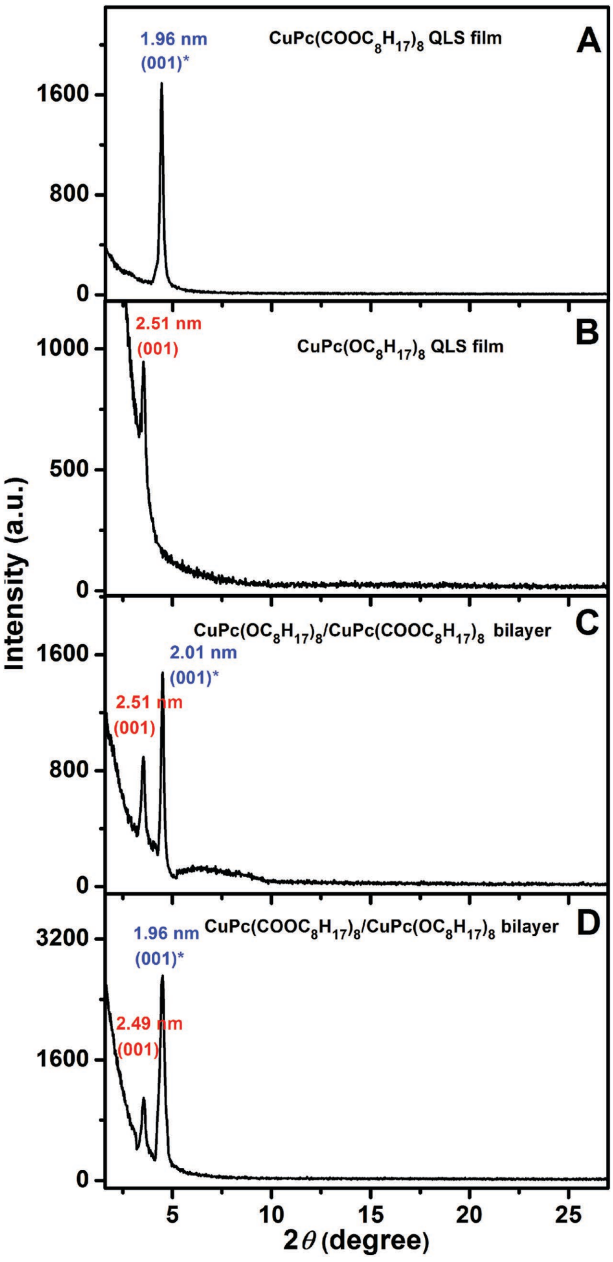

Figure 3. X-ray patterns for the A) $CuPc(COOC_8H_{17})_8$ QLS film, B) $CuPc(OC_8H_{17})_8$ QLS film, C) $CuPc(OC_8H_{17})_8/CuPc(COOC_8H_{17})_8$ bilayer (*p*/*n*-bilayer) heterojunction thin film, and D) $CuPc(COOC_8H_{17})_8/CuPc(OC_8H_{17})_8$ bilayer (*n*/*p*-bilayer) heterojunction thin film deposited on the SiO_2/Si substrates.

oriented as a slipped co-facial stack with an "edge-on" configuration (*J*-aggregates) on the substrate surface.

Figure 3C shows the OOP XRD pattern of $CuPc(OC_8H_{17})_8/CuPc(COOC_8H_{17})_8$ bilayer (*p*/*n*-bilayer) heterojunction. Two peaks corresponding to the (001) lattice plane of the top-layer and sub-layer, respectively, were observed at 2.01 nm (2θ = 4.44°) and 2.51 nm (2θ = 3.52°), indicating the existence of an ordered layer structure parallel to the substrate[7,9,26,27] in both the sub-layer and top-layer of this *p*/*n*-bilayer heterojunction film. The (001) Bragg diffraction peak due to the $CuPc(OC_8H_{17})_8$ sub-layer in the two-component *p*/*n*-bilayer heterojunction film was observed in just the same position as for its single-component film, confirming the same molecular packing model employed by the $CuPc(OC_8H_{17})_8$ molecules in the sub-layer of *p*/*n*-bilayer heterojunction with that in the single-component film. However, the (001) diffraction peak due to the $CuPc(COOC_8H_{17})_8$ top-layer of *p*/*n*-bilayer heterojunction appearing at 2.01 nm indicates a larger $CuPc(COOC_8H_{17})_8$ monolayer thickness (or periodic spacing distance) than that of its single-component QLS film (1.96 nm). This results in a higher orientation angle (≈34°) of $CuPc(COOC_8H_{17})_8$ molecular plane to the film surface, suggesting the more intense intermolecular interaction between neighboring π columnar stacks in the bilayer heterojunction, which in turn provides the π electrons (as well as holes) with a more extensive area for delocalization in the bilayer film than in the single-component QLS film[31a] and becomes responsible for the better ambipolar device performance for the *p*/*n*-bilayer OTFTs. Similar to the *p*/*n*-bilayer heterojunction thin film, two diffraction peaks due to the $CuPc(OC_8H_{17})_8$ top-layer and $CuPc(COOC_8H_{17})_8$ sub-layer were observed at 2.49 nm (2θ = 3.54°) and 1.96 nm (2θ = 4.50°), respectively, in the OOP XRD pattern of $CuPc(COOC_8H_{17})_8/CuPc(OC_8H_{17})_8$ bilayer (*n*/*p*-bilayer) heterojunction thin film (Figure 3D). Again not surprisingly at all, the same fabrication process ensures the same molecular packing model for the $CuPc(COOC_8H_{17})_8$ sub-layer in the bilayer heterojunction film as in its single-component film. However, in contrast to the *p*/*n*-bilayer heterojunction film, the monolayer thickness of the $CuPc(OC_8H_{17})_8$ top layer gets decreased in the *n*/*p*-bilayer heterojunction film (2.49 nm) relative to that in its single-component film (2.51 nm; Figure 3B,D), revealing a more slipped arrangement of the $CuPc(OC_8H_{17})_8$ molecules with a smaller orientation angle (≈49°) in the top-layer of the *n*/*p*-bilayer heterojunction film than that in the $CuPc(OC_8H_{17})_8$ single-layer film. This in turn leads to a negative impact on the carrier mobilities of the corresponding ambipolar *n*/*p*-bilayer heterojunction OTFT devices. It is worth noting that the relative intensity of the Bragg peak for either $CuPc(COOC_8H_{17})_8$ (**1**) or $CuPc(OC_8H_{17})_8$ (**2**) in $CuPc(OC_8H_{17})_8/CuPc(COOC_8H_{17})_8$ (*p*/*n*-bilayer) heterojunction gets slightly decreased in comparison with that of the single-component QLS film (Figure 3A–C) in line with that found for the vacuum-deposited CuPc/F_{16}CuPc heterojunction,[7] implying the smaller nanocrystallite size of either **1** or **2** in the *p*/*n*-bilayer than in the corresponding single-component film.[31b,c] In good contrast, the relative intensity of the Bragg peak for either **1** or **2** in $CuPc(COOC_8H_{17})_8/CuPc(OC_8H_{17})_8$ (*n*/*p*-bilayer) heterojunction gets increased in comparison with that of the single-component QLS film (Figure 3A,B,D), suggesting the larger nanocrystallite size of either **1** or **2** in the *n*/*p*-bilayer relative to the single-component film. Additional support of this point comes from the AFM measurement result as detailed below. Anyway, the smaller grain size for the *p*/*n*-bilayer than *n*/*p*-bilayer heterojunction provides a larger and more effective adsorption surface area to the analytes.[30b–d] This in turn would enhance the gas-sensing performance for the *p*/*n*-bilayer devices.

Figure 4 compares the surface morphologies between the single-component, either $CuPc(COOC_8H_{17})_8$ or $CuPc(OC_8H_{17})_8$, and two-component bilayer heterojunction films. As can be

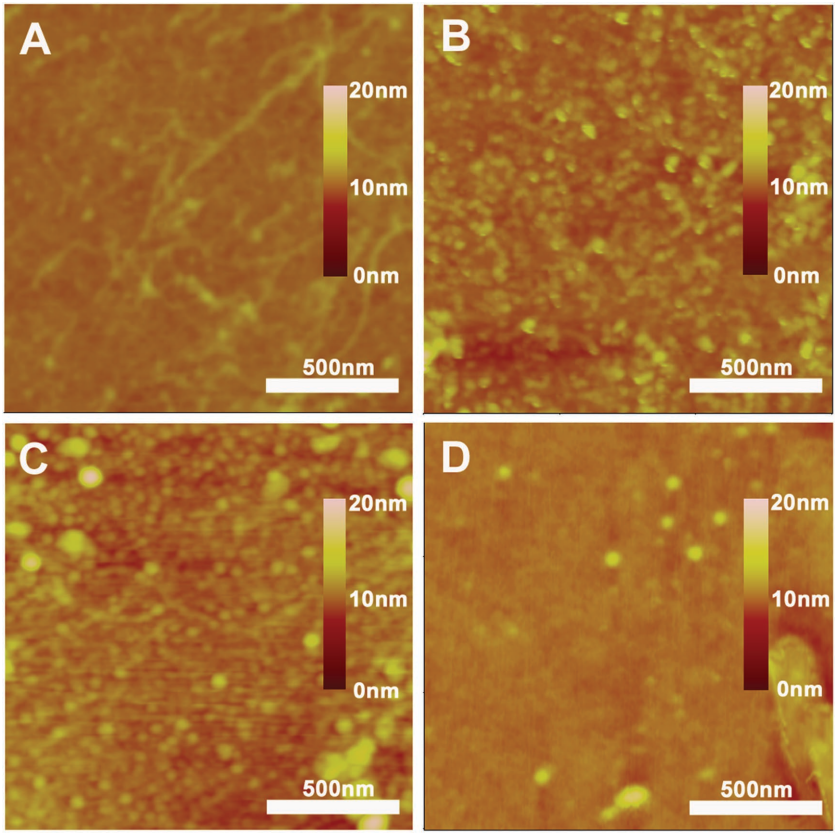

Figure 4. AFM images (height scale 20 nm) of A) $CuPc(COOC_8H_{17})_8$ QLS film, B) $CuPc(COOC_8H_{17})_8$ QLS film, C) $CuPc(OC_8H_{17})_8/CuPc(COOC_8H_{17})_8$ bilayer (*p*/*n*-bilayer) heterojunction thin film, and D) $CuPc(COOC_8H_{17})_8/CuPc(OC_8H_{17})_8$ bilayer (*n*/*p*-bilayer) bilayer heterojunction thin film grown on the HMDS-treated SiO_2/Si substrate.

seen in Figure 4A, the image for the $CuPc(COOC_8H_{17})_8$ (**1**) QLS film formed on the SiO_2/Si surface consists of small domains of ≈55 ± 15 nm in size (Figure S7, Supporting Information), giving a root-mean-square (R_{rms}) roughness value of 0.36 nm and revealing a typical smooth surface. In contrast, due to the enhanced intermolecular interaction of **2**, a relatively high R_{rms} value, 0.74 nm, was observed for the grain crystallites with the size of ≈65 ± 10 nm on the surface of $CuPc(OC_8H_{17})_8$ (**2**) QLS film (Figure 4B and Figure S7, Supporting Information). Interestingly, the surface morphology of the *p*/*n*-bilayer heterojunction film by depositing $CuPc(COOC_8H_{17})_8$ (**1**) over the $CuPc(OC_8H_{17})_8$ (**2**) sub-layer is more similar to that of $CuPc(OC_8H_{17})_8$ QLS film (Figure 4C and Figure S7, Supporting Information) rather than that of $CuPc(COOC_8H_{17})_8$ QLS film (Figure 4A) in terms of both the increased grain-like domain size (about 45 ± 15 nm) and R_{rms} value (0.49 nm). This is also true for the $CuPc(COOC_8H_{17})_8/CuPc(OC_8H_{17})_8$ bilayer (*n*/*p*-bilayer) heterojunction film (Figure 4D and Figure S7, Supporting Information), with the domain diameter of about 85 ± 25 nm and R_{rms} value of 0.35 nm. These results clearly confirm the important templating role of the sub-layer film in modulating the aggregation behavior (or molecular packing) for the top-layer molecules in the two-component bilayer heterojunctions via solution processed procedure. Obviously, the better molecular ordering within the thin films of both the top- and sub-layer of the *p*/*n*-bilayer heterojunction film than that of the *n*/*p*-bilayer heterojunction will reduce the trap states in the conductive channels and thus surely improve the charge transport, resulting in the superior device performance for the *p*/*n*-bilayer heterojunction OTFT devices over the *n*/*p*-bilayer ones.

2.4. Current–Voltage Characteristics

For the purpose of detecting the electrical contact nature between the organic thin film and electrodes, current–voltage (*I*–*V*) curves have been measured for all the devices. As shown in **Figure 5**, all the devices exhibit similar Ohmic behavior at low bias voltages, confirming the good electrical contact between the organic thin film and electrodes. However, the response gets increased in the order from *n*-type $CuPc(COOC_8H_{17})_8$, $CuPc(COOC_8H_{17})_8/CuPc(OC_8H_{17})_8$ bilayer (*n*/*p*-bilayer), $CuPc(OC_8H_{17})_8/CuPc(COOC_8H_{17})_8$ bilayer (*p*/*n*-bilayer), to *p*-type $CuPc(OC_8H_{17})_8$ QLS film. In detail, the current developed by both the $CuPc(COOC_8H_{17})_8/CuPc(OC_8H_{17})_8$ bilayer (*n*/*p*-bilayer) (in the range of 1.4×10^{-8} A) and $CuPc(OC_8H_{17})_8/CuPc(COOC_8H_{17})_8$ bilayer (*p*/*n*-bilayer) film (in the range of 2.2×10^{-8} A) is higher than that by $CuPc(COOC_8H_{17})_8$ single layer (in the range of 5.9×10^{-9} A) but lower than that by $CuPc(OC_8H_{17})_8$ single layer film (in the range of 7.2×10^{-8} A), indicating the government of the charge transfer in the two-component bilayer heterostructures by both the charge injection into the sub-layer and the

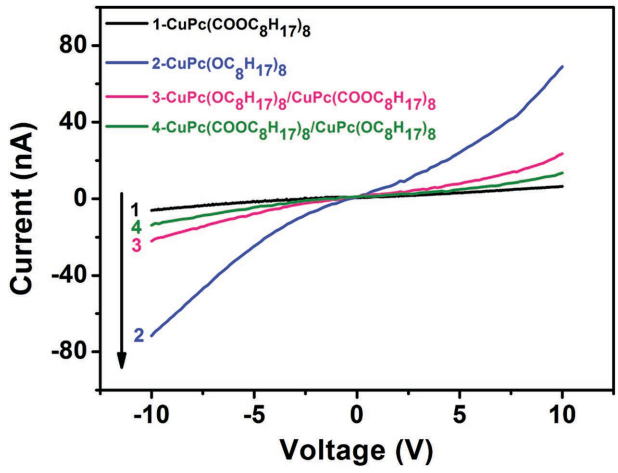

Figure 5. Representative *I*–*V* characteristics for the QLS films of *n*-type $CuPc(COOC_8H_{17})_8$, *p*-type $CuPc(OC_8H_{17})_8$, $CuPc(OC_8H_{17})_8/CuPc(COOC_8H_{17})_8$ bilayer (*p*/*n*-bilayer), and $CuPc(COOC_8H_{17})_8/CuPc(OC_8H_{17})_8$ bilayer (*n*/*p*-bilayer) films.

current flowing across the organic heterointerface (the present result seems to provide an effective method to tune the conductivity of the two-component bilayer device through changing the composition of the sub-layer). In addition, the conductivity for the single-component QLS film of **2** obtained,[21,22] $\approx 10^{-5}$ S cm^{-1}, is about 100 times bigger than that of **1**, $\approx 10^{-7}$ S cm^{-1}, indicating the significant dependence of the single-component QLS film semiconductivity on the electron withdrawing/donating nature of the phthalocyanine peripheral substituents since incorporation of electron-withdrawing substituents onto the phthalocyanine periphery leads to a decrease in the electron density of the conjugated macrocycle and an increase in the oxidation potential of the system. This result is in line with previous findings concerning the electrical behavior of MPc and $MPcF_{16}$ (M = Cu, Zn) films.[26,27,32]

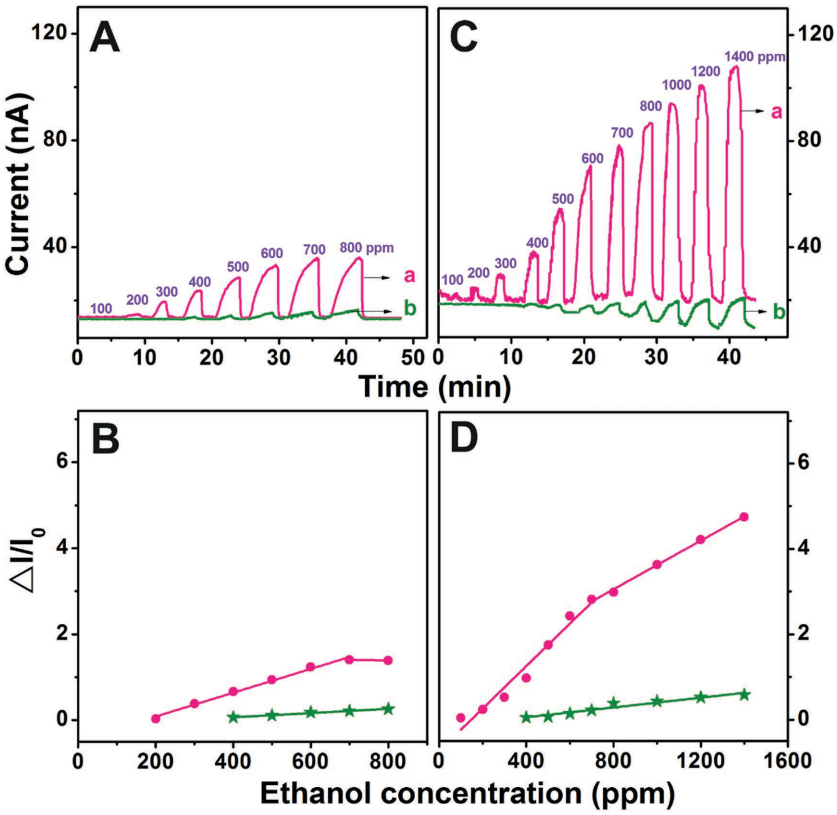

Figure 6. The time-dependent current plots (above column) and sensor response as a function of the ethanol concentration (below column) for the $CuPc(OC_8H_{17})_8/CuPc(COOC_8H_{17})_8$ bilayer (*p*/*n*-bilayer) (a) and $CuPc(COOC_8H_{17})_8/CuPc(OC_8H_{17})_8$ bilayer (*n*/*p*-bilayer) (b) QLS films deposited A,B) onto the SiO_2/Si substrates with Au electrodes and C,D) onto the glass substrates with ITO interdigitated electrodes, respectively.

2.5. Gas-Sensing Performance

To assess the gas sensing properties to ethanol of these two-component bilayer heterojunctions, responses of both $CuPc(OC_8H_{17})_8/CuPc(COOC_8H_{17})_8$ bilayer (*p*/*n*-bilayer) and $CuPc(COOC_8H_{17})_8/CuPc(OC_8H_{17})_8$ bilayer (*n*/*p*-bilayer) QLS films with Au electrodes to a series of ethanol concentration were carried out at room temperature in comparison with those of $CuPc(COOC_8H_{17})_8$ or $CuPc(OC_8H_{17})_8$ single-component QLS film. As can be seen from the time-dependent current plots shown in **Figure 6** and **Table 2**, both $CuPc(COOC_8H_{17})_8$ (**1**) and $CuPc(OC_8H_{17})_8$ (**2**) single-component sensor devices have no response to ethanol vapor under the test voltage 5 and gate voltage 0 V, respectively. In good contrast, both two-component bilayer heterojunction devices show a positive response to ethanol vapor together with good recovery characteristic at room temperature, with a duty cycle where the dynamic exposure period is fixed at 4 min and static recovery period at 1 min (Figure 6A). However, the heterojunction devices with *p*/*n*-structure display much superior sensing property to ethanol vapor over the *n*/*p*-bilayer devices in terms of sensitivity. In addition, as clearly shown in Figure 6A, upon exposure to the vapor of ethanol (with weak electron-donating nature), the conductivity of both bilayer devices gets obviously increased due to an increase in the density of electron charge carriers in the semiconducting layer of either *p*/*n*- or *n*/*p*-bilayer heterojunctions.

To quantify the sensor response, we define the relative response intensity $S = (\Delta I/I_0) \times 100\%$, where I_0 is the baseline current value and $\Delta I = I_g - I_0$; I_g is the current value when the ethanol gas is switched on.[33] As exhibited in Figure 6B, a linear relationship exists between the relative response intensity *S* and ethanol concentrations for the *n*/*p*- and *p*/*n*-bilayer heterojunctions in the range of 200–700 and 400–800 ppm with the slope (in %ppm^{-1} defined as the gas sensor sensitivity) of the linear fit of 0.28 and 0.051, respectively. Obviously, the *p*/*n*-bilayer heterojunction device with a $CuPc(OC_8H_{17})_8$ sub-layer and a $CuPc(COOC_8H_{17})_8$ top-layer shows superior sensing property to ethanol vapor to the *n*/*p*-bilayer counterpart with a $CuPc(COOC_8H_{17})_8$ sub-layer and a $CuPc(OC_8H_{17})_8$ top-layer in terms of both the sensitivity, 0.28 versus 0.051, and detection limit, 200 versus 400 ppm, due to the synergistic effect of relatively intensified charge-transfer interaction between the weak reducing ethanol molecule (as electron-donor) and more electron-deficient Cu(II) ion in $CuPc(COOC_8H_{17})_8$ on the top-layer of *p*/*n*-bilayer than that in $CuPc(OC_8H_{17})_8$ on the top-layer of *n*/*p*-bilayer device in combination with the more conductive $CuPc(OC_8H_{17})_8$ sub-layer in the former *p*/*n*-bilayer heterojunctions.[34] In addition, these results clearly indicate the effect of the bilayer structure of heterojunctions on the gas sensing behavior. At the end of this section, it is noteworthy that it is easy to understand the increase in the conductivity of the *p*/*n*-bilayer devices upon exposure to the vapor of ethanol as detailed above. This, however, is not the case for the *n*/*p*-bilayer devices. Actually, despite the failure in directly detecting the *n*-type conductivity property for the $CuPc(OC_8H_{17})_8$ (**2**) single-component film in the present case, electron transport for this compound is still possible due to the location of its LUMO energy level at 3.65 eV, quite close to that for the *n*-type

Table 2. Characteristics of the ethanol sensing behavior from two-component QLS films with Au and ITO IDEs, respectively, at room temperature.

Compound	Au electrodes				ITO electrodes			
	Detection Limit [ppm]	Sensitivity [%ppm^{-1}]	R^2 [%]	Exposure/recovery period [min/min]	Detection limit [ppm]	Sensitivity [%ppm^{-1}]	R^2 [%]	Exposure/recovery period [min/min]
p/*n*-bilayer	200	0.28	99	4/1	100	0.49/0.29	96/99	2/1
n/*p*-bilayer	400	0.051	97	4/1	400	0.057	94	2/1

semiconductor.[3c,35] As a result, along with the interaction of the top-layer CuPc(OC_8H_{17})$_8$ molecules with the vaporizing ethanol molecules with weak electron-donating nature, the concentration of electron injected near the surface of the bilayer interface gets increased. This in turn results in the positive response for the *n*/*p*-bilayer heterojunction to the ethanol vapor, too, similar to its *p*/*n*-bilayer counterparts.

It is well known that change in the working electrodes has significant effect on the nature and performance of certain organic semiconductor-based OFET devices.[36] This should be also true for the organic semiconductor-based chemiresistor, which, however, has never been demonstrated previously. As a consequence, ITO electrodes with the work function of 4.5 eV[11–13] instead of the Au electrodes with the work function of 5.1 eV were employed to fabricate the bilayer heterojunction gas sensing devices. As shown in Figure 6C, with the employment of the ITO work electrodes, both the CuPc(OC_8H_{17})$_8$/CuPc($COOC_8H_{17}$)$_8$ *p*/*n*- and *n*/*p*-bilayer heterojunction devices show improved ethanol sensing properties over that of the Au IDEs in terms of the increased wide concentration range of 100/400–1400 ppm with almost zero baseline drift with the decreased dynamic exposure period of 2 min and static recovery period of 1 min. Nevertheless, in addition to the increased ethanol gas sensor sensitivity from 0.28 to 0.49%ppm^{-1} in the original concentration range of 100–700 or 200–700 ppm, the *p*/*n*-bilayer heterojunction devices with ITO-IDEs exhibit good gas sensor sensitivity to ethanol vapor in the increased concentration range of 700–1400 ppm (0.29%ppm^{-1}). However, unlike the obvious increased concentration range to the ethanol vapor, the sensor sensitivity to ethanol vapor for the CuPc($COOC_8H_{17}$)$_8$/CuPc(OC_8H_{17})$_8$ *n*/*p*-bilayer sensors with ITO electrodes only gets slightly increased to 0.057%ppm^{-1} (Figures 6C,D). As a total result, the present result concerning the *p*/*n*-bilayer heterojunction sensor devices provides a good application potential for practical ethanol detecting due to the detection limit of the breath analyzer of 200 ppm.[14a] In addition, it is worth noting that the present result actually represents the first two-component bilayer organic heterojunction ethanol sensor with excellent sensing performance reported thus far.[37]

For the purpose of practical application, the selectivity of corresponding sensor to corresponding gas is of key importance. It has been revealed that the mouth and body odors and human breath for a drunken person also contain a number of organic species including volatile amines, acetone, toluene, and cyclohexane in addition to alcohol as the main organic content.[38] As a consequence, chemical selectivity of the ethanol sensors over acetone, cyclohexane, toluene, ammonia, and triethylamine has to be evaluated. The sensing properties of the *p*/*n*-bilayer heterojunction devices over acetone, cyclohexane, toluene, ammonia, and triethylamine were systematically investigated. As shown in Figure S8 (Supporting Information), except ethanol vapor, only at the high working temperature (120–200 °C) and a very high concentration for cyclohexane (6.6×10^4 ppm), toluene (7.3×10^4 ppm), ammonia (4.1×10^3 ppm), and triethylamine (5.4×10^4 ppm), these organic compounds can be detected. Actually at any high concentration, the *p*/*n*-bilayer heterojunction devices show no response for the acetone species. The fact that only poor response of the *p*/*n*-bilayer heterojunction sensors to the very high concentration (≈10^3–10^4 ppm) of analytes (acetone, cyclohexane, toluene, ammonia, and triethylamine at an elevated temperature (120–200 °C) confirms the excellent selectivity of the sensors. Obviously, the weak sensor–analyte interaction, which in turn determines the amount of analyte adsorbed on the surface of the *p*/*n*-bilayer heterojunction sensor, should be mainly responsible for the resulting poor sensing behaviors.[39] More interestingly, the conductivity of the *p*/*n*-bilayer heterojunction gets slightly increased upon exposure to the nonpolar cyclohexane and weak-polar toluene vapor but slightly decreased in the presence of the electron-donating triethylamine and ammonia vapors (Figure S8, Supporting Information). Considering the *n*-type nature of the top CuPc($COOC_8H_{17}$)$_8$ layer of this *p*/*n*-bilayer heterojunction, such an obvious *p*-type response to the donor species in the heterojunction devices is indeed strange at the first glance, which however could be rationalized on the basis of the ambipolar semiconducting characteristics of the *p*/*n*-bilayer heterojunction. Nevertheless, this result seems to suggest that the semiconducting nature (*n*-type vs *p*-type) of the ambipolar organic sensing materials is able to change depending on the electron-donating abilities of the analyte molecules adsorbed on the surface of the *p*/*n*-bilayer heterojunction sensors. However, weak electron-donating ability of acetone in combination with the lack of enough intermolecular interactions between acetone and semiconducting layer should be responsible for the totally no sensitivity of the *p*/*n*-bilayer heterojunction sensors to acetone.

3. Conclusion

Briefly summarizing above, novel two-component bilayer heterojunctions with both *p*/*n*- and *n*/*p*-structures have been successfully fabricated from *p*-type CuPc(OC_8H_{17})$_8$ and *n*-type CuPc($COOC_8H_{17}$)$_8$ by a simple two-step solution-processed QLS method. Due to the important templating role of the sub-layer film for the top-layer, the two-component heterojunction OTFTs with CuPc(OC_8H_{17})$_8$ as sub-layer with a more ordered and densely packed molecular architecture in the QLS film

exhibited superior air-stable ambipolar device performance over the ones with CuPc($COOC_8H_{17}$)$_8$ as sub-layer, with the hole and electron mobility of 0.11 and 0.02 $cm^2\ V^{-1}\ s^{-1}$. In particular, excellent sensing property with good selectivity and reversibility, low detection limit, and high sensitivity for ethanol vapor in the range of 100–1400 ppm at room temperature was revealed for the *p*/*n*-bilayer heterojunction devices with ITO IEDs, showing the great application potential for the practical ethanol detection.

4. Experimental Section

Materials and Chemicals: Both 2,3,9,10,16,17,24,25-octakis(octyloxycarbony) phthalocyaninato copper compound CuPc($COOC_8H_{17}$)$_8$ (**1**) and 2,3,9,10,16,17,24,25-octakis(octyloxy)phthalocyaninato copper compound CuPc(OC_8H_{17})$_8$ (**2**) were synthesized following the published procedure[18,19] and characterized by the matrix-assisted laser desorption/ionization time-of-flight mass, IR, and electronic absorption spectra in addition to elemental analysis (Figures S9 and S10, Supporting Information). All other reagents and solvents were of reagent grade and used as received.

Fabrication of the Bilayer Heterojunctions: Two-component bilayer heterojunction films were built by a two-step QLS procedure (Scheme 2). (i) The preparation of the sub-layer (or single-layer): the chloroform solution of the sample (**1** or **2**, $\approx 1 \times 10^{-6}$ mol L^{-1}) was put into a cylindrical glass container, then water was slowly added onto the surface of the chloroform solution in the container (caution: the amount of water added should not completely cover the surface of the chloroform solution so as to keep the path for the evaporation of the $CHCl_3$ solvent). During the solvent evaporation, the molecules gradually assembled to form some fine nanostructures at the $CHCl_3$/water interface. After complete evaporation of $CHCl_3$, the densely packed film remained on the water surface, and then the film was transferred onto the quartz, ITO/glass, or SiO_2/Si substrate by horizontal lifting.[26] This process was repeated to obtain the required number of layers. Residual water on the substrate, between transfer steps and after the final transfer, was removed with a stream of N_2. (ii) The preparation of the two-component bilayer heterojunction: the densely packed film of another sample (**2** or **1**) formed on the water surface was transferred via repeating the deposition (QLS film) onto the newly prepared film of the sample (**1** or **2**) in step (i), resulting in the two-component bilayer heterojunction films with either *p*/*n*- or *n*/*p*-structure. In the present case, the semiconducting active-layers were deposited at a constant number of 20-layer QLS film in both the single-component films and two-component bilayer films (10-layer for each of **1** and **2**) at room temperature.

Fabrication and Measurements of OTFT and Sensor Devices: OTFT devices were fabricated on an HMDS-treated SiO_2/Si (300 nm thickness, capacitance C_0 = 10 nF cm^{-2}) substrate by evaporating gold electrodes onto the single-component and two-component QLS films employing a shadow mask. These electrodes have a width (W) of 28.6 mm and a channel length (L) of 0.24 mm. The ratio of the width to length (W/L) of the channel was then 119. The drain–source current (I_{ds}) versus drain–source voltage (V_{ds}) characteristic was obtained with a Hewlett-Packard (HP) 4140B parameter analyzer at room temperature. Experimental data were analyzed using standard field-effect transistor equations: $I_{ds} = (W/2L)\mu C_0(V_g - V_T)^2$, where I_{ds} is the source–drain current, V_g is the gate voltage, C_0 is the capacitance per unit area of the dielectric layer, V_T is the threshold voltage, and μ is the mobility on the saturation region.[18] The mobility (μ) and threshold voltage (V_T) can then be calculated from the slope and intercept of the linear part of the V_g versus $(I_{ds})^{1/2}$ plot.

In addition to the OTFT devices that were used directly as ethanol sensors, another kind of sensor devices were built by depositing two-component QLS films onto the ITO/glass IDEs. The ITO/glass IDEs are composed of ten pairs of digits deposited on glass substrate with the following dimensions: 0.125 mm electrode width, 0.075 mm spacing, 6 mm overlapping length, and 20 nm electrode thickness. Prior to the deposition, substrates were successively sonicated in methylbenzene, acetone, ethanol, and distilled water, respectively, which were finally dried with N_2 gas for about 30 s (average three times). The ethanol-sensing properties of the devices were examined by exposing the corresponding films to different concentrations of ethanol and measuring the current changes of the films at a constantly polarized voltage of 5 V.

Characterization: Electrochemical measurement was carried out with a CHI760D voltammetric analyzer. The cell comprised inlets for a glassy carbon disk working electrode of 3.0 mm in diameter and a silver wire counter electrode. The reference electrode was Ag/Ag^+ (0.01 mol dm^{-3}), which was connected to the solution by a Luggin capillary, whose tip was placed close to the working electrode. It was corrected for junction potentials by being referenced internally to the ferrocenium/ferrocene (Fe^+/Fe) couple [$E_{1/2}$ (Fe^+/Fe) = 0.50 V vs SCE]. Typically, a 0.1 mol dm^{-3} solution of [Bu_4N][ClO_4] in CH_2Cl_2 containing 0.5 mmol dm^{-3} of sample was purged with nitrogen for 5 min, then the voltammogram was recorded at ambient temperature. Electronic absorption spectra were recorded on a Hitachi U-4100 spectrophotometer (scan speed: 600 nm min^{-1}, sampling interval: 1.00 nm, slit width: 4.00 nm, wavelength resolution: 0.15 nm, beam size: 0.2 nm, response time: 1 s). X-ray diffraction experiment was carried out on a Bruker D8 ADVANCE X-ray diffractometer using Cu Kα radiation (λ = 1.5406 Å) with scattering angles (2θ) of 1.6°–30°. The accelerating voltage and the applied current were 40 KV and 40 mA, respectively. Data were recorded at a scan rate of 0.02° 2θ s^{-1} (beam size: 1 × 10 mm; detector type: lynxeye detector). AFM images were collected under ambient conditions using the tapping mode with a NanoscopeIII/Bioscope scanning probe microscope from Digital instruments. Tapping mode AFM images were obtained under the scale height of 200 nm and scale phase of 100 nm as well as set point amplitude of 1.00 Hz.

Supporting Information

Supporting Information is available from the Wiley Online Library or from the author.

Acknowledgements

This work was financially supported by the Natural Science Foundation of China (Grant Nos. 21290174 and 21371073), the National Key Basic Research Program of China (Grant Nos. 2013CB933402 and 2012CB224801) and the Fundamental Research Funds for the Central Universities.

Received: March 25, 2016
Revised: May 27, 2016
Published online:

[1] a) C. D. Dimitrakopoulos, P. R. L. Malenfant, *Adv. Mater.* **2002**, *14*, 99; b) H. Sirringhaus, *Adv. Mater.* **2005**, *17*, 2411; c) R. J. Li, W. P. Hu, Y. Q. Liu, D. B. Zhu, *Acc. Chem. Res.* **2010**, *43*, 529; d) H. Usta, A. Facchetti, T. J. Marks, *Acc. Chem. Res.* **2011**, *44*, 501; e) L. Valli, *Adv. Colloid Interface Sci.* **2005**, *116*, 13.

[2] a) H. Usta, C. Risko, Z. M. Wang, H. Huang, M. K. Deliomeroglu, A. Zhukhovitskiy, A. Facchetti, T. J. Marks, *J. Am. Chem. Soc.* **2009**, *131*, 5586; b) P. Sonar, S. P. Singh, Y. N. Li, M. S. Soh, A. Dodabalapur, *Adv. Mater.* **2010**, *22*, 5409.

[3] a) Y. L. Chen, D. P. Li, N. Yuan, J. Gao, R. M. Gu, G. F. Lu, M. Bouvet, *J. Mater. Chem.* **2012**, *22*, 22142; b) D. P. Li, H. L. Wang, J. L. Kan, W. J. Lu, Y. L. Chen, J. Z. Jiang, *Org. Electron.* **2013**, *14*, 2582; c) J. L. Kan, Y. L. Chen, D. D. Qi, Y. Q. Liu, J. Z. Jiang, *Adv. Mater.* **2012**, *24*, 1755.

[4] J. Zaumseil, H. Sirringhaus, *Chem. Rev.* **2007**, *107*, 1296.
[5] R. B. Ye, M. Baba, K. Suzuki, K. Mori, *Solid-State Electron.* **2008**, *52*, 60.
[6] A. Dodabalapur, H. Katz, L. Torsi, R. Haddon, *Science* **1995**, *269*, 1560.
[7] J. Wang, H. B. Wang, X. J. Yan, H. C. Huang, D. Jin, J. W. Shi, Y. H. Tang, D. H. Yan, *Adv. Funct. Mater.* **2006**, *16*, 824.
[8] Z. M. Wei, W. Xu, W. P. Hu, D. B. Zhu, *Langmuir* **2009**, *25*, 3349.
[9] D. M. Gao, X. Zhang, X. Kong, Y. L. Chen, J. Z. Jiang, *ACS Appl. Mater. Interfaces* **2015**, *7*, 2486.
[10] a) H. L. Dong, X. L. Fu, J. Liu, Z. R. Wang, W. P. Hu, *Adv. Mater.* **2013**, *25*, 6158; b) S. Z. Bisri, C. Piliego, J. Gao, M. A. Loi, *Adv. Mater.* **2014**, *26*, 1176; c) O. A. Melville, B. H. Lessard, T. P. Bender, *ACS Appl. Mater. Interfaces* **2015**, *7*, 13105.
[11] B. P. J. D. L. Costello, R. J. Ewen, H. E. Gunson, N. M. Ratcliffe, P. T. N. Spencer-Phillips, *Meas. Sci. Technol.* **2000**, *11*, 1685.
[12] W. Zeng, T. M. Liu, Z. C. Wang, *Mater. Trans.* **2010**, *51*, 243.
[13] J. J. Ho, Y. K. Fang, K. H. Wu, W. T. Hsieh, C. H. Chen, M. S. Ju, J. J. Lin, S. B. Hwang, *Sens. Actuators B* **1998**, *50*, 227.
[14] a) J. F. Liu, X. Wang, Q. Peng, Y. D. Li, *Adv. Mater.* **2005**, *17*, 764; b) R. N. Mariammal, K. Ramachandran, B. Renganathan, D. Sastikumar, *Sens. Actuators B* **2012**, *169*, 199; c) F. X. Zhang, *Sensor Application and its Circuit Selection, Publishing House of Chinese Electronics Industry,* Beijing, China **1993**, 561.
[15] a) E. J. Meijer, D. M. de Leeuw, S. Setayesh, E. van Veenendaal, B. H. Huisman, P. W. M. Blom, J. C. Hummelen, U. Scherf, T. M. Klapwijk, *Nat. Mater.* **2003**, *2*, 678; b) A. M. Zhong, Y. Z. Bian, Y. X. Zhang, *J. Phys. Chem. C* **2010**, *114*, 3248.
[16] H. Usta, C. Risko, Z. Wang, H. Huang, M. K. Deliomeroglu, A. Zhukhovitskiy, A. Facchetti, T. J. Marks, *J. Am. Chem. Soc.* **2009**, *131*, 5586.
[17] Y. L. Guo, G. Yu, Y. Q. Liu, *Adv. Mater.* **2010**, *22*, 4427.
[18] P. Ma, J. L. Kan, X. Zhang, C. H. Hang, Y. Z. Bian, Y. L. Chen, N. Kobayshi, J. Z. Jiang, *J. Mater. Chem.* **2011**, *21*, 18552.
[19] X. Y. Wang, X. Zhang, X. Sun, Y. Z. Bian, C. Q. Ma, J. Z. Jiang, *Inorg. Chem.* **2007**, *46*, 7136.
[20] a) Y. X. Zhang, X. X. Zhang, Z. Q. Liu, Y. Z. Bian, J. Z. Jiang, *J. Phys. Chem. A* **2005**, *109*, 6363; b) M. Kasha, H. R. Rawls, M. A. El-Bayoumi, *Pure Appl. Chem.* **1965**, *11*, 371.
[21] Y. Chen, M. Bouvet, T. Sizun, Y. N. Gao, C. Plassard, E. Lesniewska, J. Z. Jiang, *Phys. Chem. Chem. Phys.* **2010**, *12*, 12851.
[22] J. Gao, G. F. Lu, J. L. Kan, Y. L. Chen, M. Bouvet, *Sens. Actuators B* **2012**, *166–167*, 500.
[23] A. W. Snow, W. R. Barger, *Phthalocyanines: Properties and Applications*, (Eds: C. C. Leznoff, A. B. P. Lever), Wiley-VCH, Weinheim, Germany **1989**, 341.
[24] a) B. Jancy, S. K. Asha, *Chem. Mater.* **2008**, *20*, 169; b) H. X. Wu, L. Xue, Y. L. Chen, X. Y. Li, *Langmuir* **2011**, *27*, 3074; c) F. Würthner, T. E. Kaiser, C. R. Saha-Möller, *Angew. Chem. Int. Ed.* **2011**, *50*, 3376.
[25] J. Wang, H. B. Wang, X. J. Yan, H. C. Huang, D. H. Yan, *Appl. Phys. Lett.* **2005**, *87*, 093507.
[26] V. Parra, J. Brunet, A. Pauly, M. Bouvet, *Analyst* **2009**, *134*, 1776.
[27] Y. L. Chen, M. Bouvet, T. Sizun, G. Barochi, J. Rossignolb, E. Lesniewska, *Sens. Actuators B* **2011**, *155*, 165.
[28] a) J. F. Liu, K. Z. Yang, Z. H. Lu, *J. Am. Chem. Soc.* **1997**, *119*, 11061; b) K. Xiao, Y. Liu, G. Yu, D. Zhu, *Appl. Phys. A* **2003**, *77*, 367.
[29] a) T. Yamamoto, H. Kokubo, M. Kobubo, M. Kobashi, Y. Sakai, *Chem. Mater.* **2004**, *16*, 4616; b) A. Monshi, M. R. Foroughi, M. R. Monshi, *World J. Nano Sci. Eng.* **2012**, *2*, 154; c) P. Smolenyak, R. Peterson, K. Nebesny, M. Törker, D. F. O'Brien, N. R. Armstrong, *J. Am. Chem. Soc.* **1999**, *121*, 8628.
[30] a) M. Yoneyama, M. Sugi, M. Saito, K. Ikegami, S. Kuroda, S. Iizima, *Jpn. J. Appl. Phys.* **1986**, *25*, 961; b) J. Q Xu, Q. Y. Pan, Y. A. Shun, Z. Z. Tian, *Sens. Actuators B* **2000**, *66*, 277; c) M. Kruk, M. Jaroniec, *Chem. Mater.* **2001**, *13*, 3169; d) J. C. Groen, L. A. A. Peffer, J. Pérez-Ramírez, *Microporous Mesoporous Mater.* **2003**, *60*, 1.
[31] a) Y. Zhao, Y. L. Guo, Y. Q. Liu, *Adv. Mater.* **2013**, *25*, 5372; b) A. Monshi, M. R. Foroughi, M. R. Monshi, *World J. Nano Sci. Eng.* **2012**, *2*, 154; c) P. Smolenyak, R. Peterson, K. Nebesny, M. To1rker, D. F. O'Brien, N. R. Armstrong, *J. Am. Chem. Soc.* **1999**, *121*, 8628.
[32] a) Z. N. Bao, A. J. Lovinger, A. Dodabalapur, *Appl. Phys. Lett.* **1996**, *69*, 3066; b) D. G. Oteyza, E. Barrena, J. O. Ossó, S. Sellner, H. Dosch, *J. Am. Chem. Soc.* **2006**, *128*, 15052; c) R. Murdey, N. Sato, M. Bouvet, *Mol. Cryst. Liq. Cryst.* **2006**, *455*, 211.
[33] S. L. Ji, H. Wang, T. B. Wang, D. H. Yan, *Adv. Mater.* **2013**, *25*, 1755.
[34] a) A. Hierlemann, A. J. Ricco, K. Bodenhöfer, W. Göpel, *Anal. Chem.* **1999**, *71*, 3022; b) F. I. Bohrer, A. Sharoni, C. Colesniuc, J. Park, I. K. Schuller, A. C. Kummel, W. C. Trogler, *J. Am. Chem. Soc.* **2007**, *129*, 5640.
[35] a) M. L. Tang, A. D. Reichardt, P. Wei, Z. N. Bao. *J. Am. Chem. Soc.* **2009**, *131*, 5264; b) J. Zaumseil, H. Sirringhaus, *Chem. Rev.* **2007**, *107*, 1296.
[36] Q. X. Tang, H. X. Li, Y. L. Liu, W. P. Hu, *J. Am. Chem. Soc.* **2006**, *128*, 14634.
[37] a) A. Yazıcı, N. Dalbul, A. Altındal, B. Salih, Ö. Bekaroğlu, *Sens. Actuators B* **2014**, *202*, 14; b) E. Kakıa, A. R. Özkayaa, A. Altındalb, B. Salihc, Ö. Bekaroğlud, *Sens. Actuators B* **2013**, *188*, 1033.
[38] a) S. van den Velde, M. Quirynen, P. van Hee, D. van Steenberghe, *Anal. Chem.* **2007**, *79*, 3425; b) S. J. Choi, B. H. Jang, S. J. Lee, B. K. Min, A. Rothschild, I. D. Kim, *ACS Appl. Mater. Interfaces* **2014**, *6*, 2588; c) Y. Ogimoto, R. Selyanchyn, N. Takahara, S. Wakamatsu, S. W. Lee, *Sens. Actuators B* **2015**, *215*, 428.
[39] M. Bora, D. Schut, M. A. Baldo, *Anal. Chem.* **2007**, *79*, 3298.